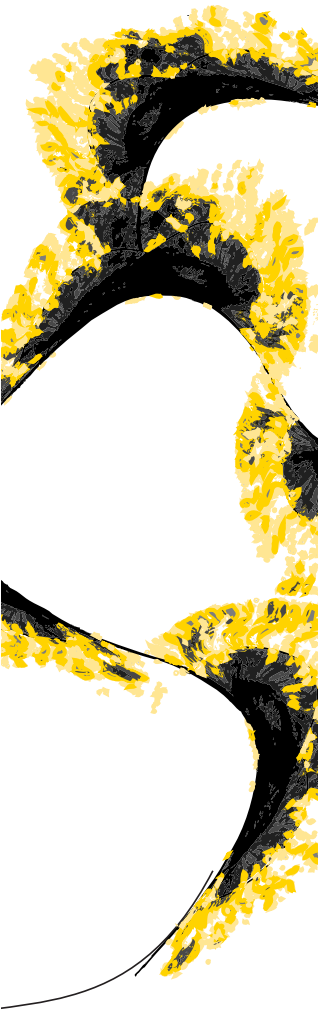

RAM ROBOTICS AND MECHATRONICS

NEW FORCE SENSORS THAT CAN BE EMBEDDED IN A SOFT ROBOTICS ACTUATOR USING 3D PRINTERS

S.T. (Syte) Veersma

BSC ASSIGNMENT

Committee:
prof. dr. ir. G.J.M. Krijnen
dr. ir. G.J.W. Wolterink
prof. dr. ir. M. Odijk

September, 2023

052RaM2023
Robotics and Mechatronics
EEMCS
University of Twente
P.O. Box 217
7500 AE Enschede
The Netherlands

UNIVERSITY OF TWENTE. | TECHMED CENTRE UNIVERSITY OF TWENTE. | DIGITAL SOCIETY INSTITUTE

Abstract

With soft robotics, the aim is to create soft robots that are flexible and can adapt to any situation. Developments in 3D printing technology allows us to create such soft robots with embedded sensors using 3D printers.
This report shows the design, fabrication and working of a 3D printed soft robotic actuator beam with embedded strain gauge sensors for contact force sensing. All sensors have a bottom and top part, so that differential measurements can be done. The embedded sensors do a total of 7 voltage measurements so that area of contact can be determined. The beam and embedded sensors have been fabricated in one go using a multi material FFF 3D printer.
The fabricated and tested actuator is able to sense contact forces with the environment. The embedded piezoresistive sensors are capable of monitoring the area of contact, using differential measurements. The sensors show a reasonable linear relation to applied forces. The actuator was made after a model based upon Euler Bernouilli beam theory. However, the experimental results mismatched the theoretical model, most likely due to this theory not made for large beam deflections.

Contents

1 Introduction

1.1 Context

Robotics is a subject that has had the attention of academics for quite a long time now. A field of research within robotics is soft robots, which has received a vast increase in interest in recent years [1]. With soft robots the aim is to create flexible and versatile robots. Because, even though existing robotic systems already have the capacity to outclass living organisms for specific mobility or environment manipulation tasks, existing robotic systems lack the versatility that a human or animal can bring [2]. Their ability to adapt to situations and environments makes soft robots safer for use, especially in interactions with humans. An example of an area where this characteristic is proven to be most valuable is in the medical field [3].

Over the last few years, 3D printers have seen a strong rise in use cases. They have been proven to be effective devices for the creation of electronic sensors. This enables 3D printers to create quick and cheap prototypes. As time passes, more and more advanced materials become available for use in 3D printing. As has been shown by Kolkman et al. [4], soft, flexible electroconductive materials can be used for creating embedded 3D printed sensors. Multi-material 3D printing allows for the embedding of sensors using these materials into soft robots in one process. This facilitates the fabrication process significantly. Printing can be done a lot faster because setup of the printer has to be done only once and no cooling between prints is required.

1.2 Related work

There are multiple works on soft robotic actuators and their sensing abilities. Some closely related papers are discussed. There are a couple of papers from the Robotics and Mechatronics (RaM) group at the University of Twente that are interesting. The first of which is by Schouten et al. [5] on different extrusion techniques for 3D printed sensors. It also shows a solution for the nonlinearity that strain sensors can have, by taking differential measurements. In a paper by Elgeneidy et al. [6] the same problem was solved by measuring regression of the actuator. Most important is the base of this research, the soft robotics actuator as designed by Kolkman et al. [4]. This actuator is capable of determining it's position using a differential pair of strain gauges, but only in an unloaded state (e.g. not applying a force on any external object).
Examples of soft robotic actuators with contact sensing exist as well. One of such is the actuator by Aljaber et al. [7]. This actuator uses multiple waveguides to sense contact with the environment. This design has the drawback of a restriction in bending angle, because of the higher stiffness of the waveguides.

1.3 Objectives

The aim of this bachelor assignment is to design a pneumatic actuator that is able to sense it's bending angle as well as interaction forces with the environment. This design should improve upon the actuator designed by Kolkman et al. [4]. The added interaction force sensors can be used to tell the actuator the point of contact with the environment, which can be used for more precise control of the actuator. This leads to the main research question:

"How to sensorize a 3D printed soft robotic actuator to capture the interaction forces with the environment."

To help answer the research question, the following sub questions can be answered.

- What materials can best be used for the sensorization of a 3D printed soft robotic actuator?

- What kind of sensor can sense the interaction force with the environment?
- How can this sensor best be integrated into the soft robotic actuator?
- How accurately can this sensor distinguish interaction forces with the environment?

1.4 Report structure

This report is built up in seven chapters. The first chapter is this short introduction to the problem and the goals of this research. The second chapter covers the current actuator design and the proposed new sensor design. The third chapter will discuss all the important theoretical and practical background. In the fourth chapter the measurements and their setup will be discussed in detail. In chapter five, the results of these measurements will be presented. The sixth chapter will give a discussion on the results and the expectations/goals. The last chapter will give a short summary of the previous chapters and will review the research question and the general results.

2 Sensor design

2.1 Introduction

This chapter will explain the process of the design of a specific soft robotic actuator with interaction force sensors. First of all, the requirements of the actuator and the integrated sensors will be formulated. After that the current actuator design will be presented and analysed, based on which a new actuator design will be presented, according to the new requirements. This new design will be described in detail, where the current design will be described more plainly. After the sensor structure is determined and the design is finished, a beam model is derived for estimating the amount of strain in the beam.

2.2 Requirements

The new design should reach the goal of "Allowing a soft robotic actuator with embedded sensing to capture and control the interaction forces with the environment" according to the research question stated in chapter 1.

1. The sensors on the actuator should be able to differentiate at least three contact points from each other
2. The sensing structure should still be able to measure the bending angle
3. The actuator should be created with 3D printing in one go

2.3 Current design

The design of the new actuator is based for the largest part on the pneumatic actuator made by Kolkman et al. [4]. This actuator was 3D printed using multi material printing. It was able to changing the bending angle of the actuator by regulating the input pressure.

2.3.1 Pneu-net actuator

One of the most developed pressure controlled soft actuators is the so called pneu-net actuator. According to [8] this class of actuator was first developed by the Whitesides Research group at Harvard University. This actuator is built up from a series of inflatable chambers, which inside walls will expand when pressure is applied. This expansion forces the chamber walls to press against each other and makes the actuator bend. Depending on how much pressure is applied, the bending angle will vary accordingly. There are two types when it comes to pneu-nets: slow pneu-nets and fast pneu-nets [9]. Figure 2.1 gives an image of how a fast pneu-net works. Only the fast pneu-net type has been shown, as the existing actuator by Kolkman et al. [4] is of that type.

2.3.2 Design

In figure 2.2 the model of the actuator with the sensing structure attached is shown. The shape of the sensing structure is shown in figure 2.3. As can be seen in figure 2.2, the sensing structure consists of two layers.

The optimal dimensions of this design are based on the actuator by Mosadegh et al. [9]. Because of the requirement of 3D printing the actuator using an FFF 3D printer, some changes had to be made. This is a fast pneu-net actuator, characterised by the fact that the chamber walls are not intra connected. However, the gaps between the chamber walls are made as small as possible to create the largest possible bending angle.

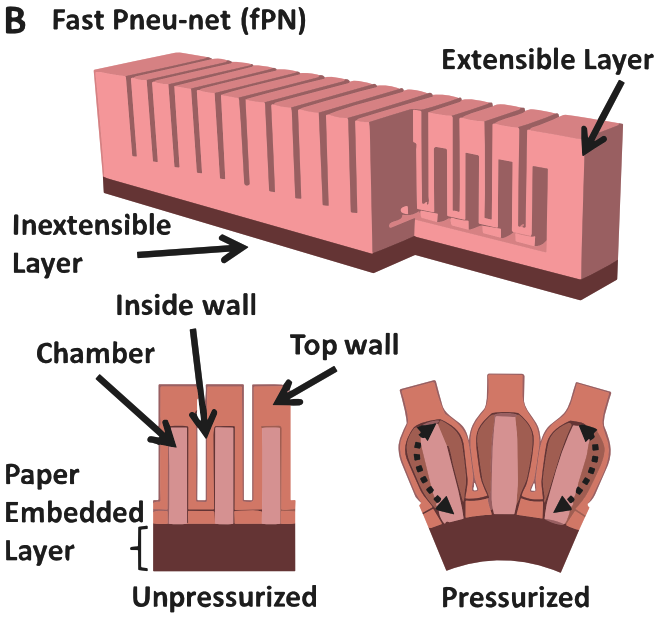

Figure 2.1: Design of a fast pneu-net by Mosadegh et al. [9]

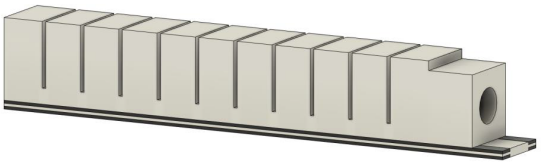

Figure 2.2: Design of the old actuator by Kolkman et al. [4] with the actuator shown in grey and the sensing material in black

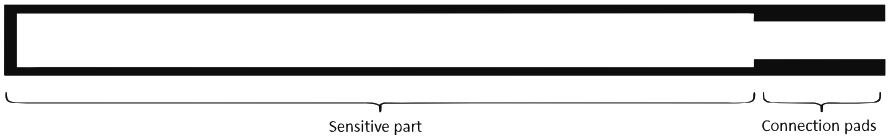

Figure 2.3: Sensing structure shape

2.3.3 Materials

For this soft actuator to function properly, the right materials have to be used. The actuator has to consist of at least two materials, a regular flexible material and a flexible electrically conductive material. Ninjaflex TPU [10] has been used as the flexible material in the actuator. This material is a quite strong but flexible filament used in fused filament fabrication 3D printing. It has a hardness of 85 shore A, which is comparable to leather. The Young's modulus of Ninjaflex is 12 MPa, which is about 10 times higher than natural rubber, and 10 times lower than leather. An alternative for Ninjaflex is X60, which is an even softer and thus more flexible material, with a 60 shore A hardness. For the electrically conductive material PI-ETPU 85-700+ [11] was used. This is a TPU filament that has been infused with carbon black particles. This makes the material almost as flexible as the Ninjaflex, with an identical Young's modulus and a similar hardness, but it is electrically conductive to a degree as well, with a resistivity of 2.8 Ωm. The similar flexibility of Ninjaflex and PI-ETPU 85-700+ is why Ninjaflex was chosen over X60 as the flexible non-conductive material. This makes it a very useful material that can be used for piezoresistive sensors, as it is conductive and flexible enough to monitor a clear resistance

change when the material is bent. To prevent the sample from sticking too much or too little to the printing bed, a support material was used. The support material that was used is PVA [12]. This is a material that is water-soluble. This means it can be removed easily, without damaging the sample, after printing.

2.4 New design

To enhance the existing actuator, it should be able to sense contact with other objects in order to inform the control scheme, so that the actuator can be controlled with more precision and safety. For this task, three types of sensors have been brought up: a capacitive sensor, an inductive sensor, or a piezoresistive sensor. Depending on which suits the requirements better, the type of sensor will be chosen.

2.4.1 Capacative sensor

Capacitive sensors can be used to sense a variety of different effects, which include force or pressure. These sensors use two parallel objects with a dielectric in between. These objects can have any shape. It is possible to create such a sensor with 3D printing, as Schouten et al. [5] have shown. The benefit of this sensor type is that they show relatively small drift, hysteresis and nonlinearity. However, these sensors are susceptible to parasitic capacitances.

2.4.2 Inductive sensor

According to Jonkers et al. [13] it is possible to create inductive sensors using 3D printing. However, due to the high resistivity of conductive 3D printing materials it is hard to create an inductive sensor with a good quality factor. With this downside, it can be concluded that other types of sensors would be more preferable.

2.4.3 Piezoresistive sensor

Piezoresistive sensors are quite often found in applications such as pressure sensors or strain gauges. These sensors use the change in electrical resistance of a material when it is stretched or compressed. This type of sensor has many benefits. It has a good sensitivity, even when working with very little stretching they can be used. Next to that, these sensors can be made on a small scale, as the only requirement for a piezoresitive sensor to work is a conductive track. Another benefit is that, as mentioned before, this kind of sensor is very easily integrated into a 3D printed object with the use of the PI-ETPU 85-700+ printing material. The main downsides to this type of sensor with this material is that it experiences drift and hysteresis and has a nonlinear resistance-strain relation. This can be partly compensated for by using differential measurement [5]. Figure 2.3 shows a piezoresistive type sensor, as it was also used in the existing actuator [4].

2.4.4 Design

Having considered each of these types of sensing principles, the choice was made to implement a piezoresistive sensor for the new actuator model. This choice was based on the fact that a piezoresistive sensor is very easy to implement in the structure of the actuator. The next best thing would have been a capacitive sensor. However, shielding such a sensor could be troublesome with limited available space. For both methods, the question remains if a sensor would be sensitive enough to monitor the force properly below 0.5 N. Choosing a piezoresistive sensor does mean that a compensation for drift, hysteresis and nonlinearities has to be implemented. Because the original actuator already uses a differential pair of sensors, the new sensors can be implemented in a comparable way.

Differential measurement

As mentioned before, 3D printed sensors using PI-ETPU show a level of drift, hysteresis and non-linearities that are unfit for a sensor working at the desired resolution. Figure 2.4 shows a clear nonlinear relation in the relative resistance change depending on the applied strain. Where the gauge factor is mostly linear until a strain of 0.05, the gauge factor goes towards zero afterwards. Qi et al. [14] had the idea that the resistance drop at a low strain was likely due to the fact that networks of conductive carbon black particles in the ETPU material are formed. When the strain rises, these networks are then broken down, which leads to an increase in resistance.

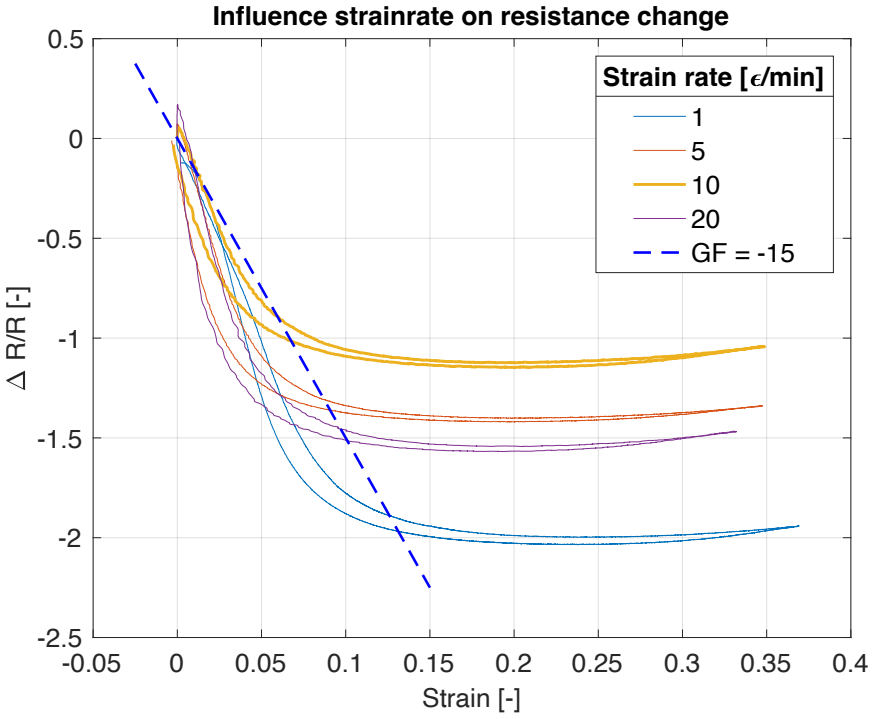

Figure 2.4: Relative resistance change of PI-ETPU versus the strain rate. Adapted from Wolterink et al. [15]

An intuitive way of solving this issue is by taking a differential measurement. Schouten et al. [16] successfully used this method to linearize a 3D printed piezoresistive tactile sensor. A differential measurement is done by measuring one parameter twice, but with opposite sign. This can be seen as [16]:

$$y_1 = f(x) \tag{2.1}$$

$$y_2 = f(-x) \tag{2.2}$$

In this case y_1 and y_2 are the sensor outputs and x the sensor input. An approximation for this can be done with a power series [4]:

$$y_1(x) = \sum_{n=0}^{\infty} a_n x^n \tag{2.3}$$

$$y_2(x) = \sum_{n=0}^{\infty} a_n (-x)^n \tag{2.4}$$

The differential measurement can then be represented by:

$$z = y_1(x) - y_2(-x) \tag{2.5}$$

$$z = \sum_{n=0}^{\infty} a_n x^n - \sum_{n=0}^{\infty} a_n (-x)^n \tag{2.6}$$

$$z = \sum_{n=0}^{\infty} 2a_n x^{2n+1} \tag{2.7}$$

Equation 2.6 shows that for all even powers, the signals cancel each other out. Removing these terms improves the linearity of the sensor. The only assumption made in this method is that both sensors have exactly the same properties. That is why the printing process should be as symmetrical as possible and the sensors should be checked for differences in properties, especially the resistances.

Structure concept

The concept for the contact sensor is as follows: there is an outer strain gauge that bends along with the rest of the actuator, much like the strain gauge in figure 2.3. Then, inside of this strain gauge three wires are connected: one at a third of the length of the strain gauge, one at two thirds of the length and one at the full length of the strain gauge. One of the first concepts made with this design idea in mind can be seen in figure 2.5.

Figure 2.5: One of the first designs for the sening structure

This version of the sensing structure had multiple issues, that have mostly been solved over numerous different iterations of concept models. The most notable thing in this design is the added strain gauge independent from the angle sensing strain gauge. However, it proved possible to use the outer strain gauge for angle measurements, while the interaction force wires are attached. This makes the inner strain gauge redundant. Additionally, it proved impossible to attach connectors to the wires using this design. That meant individual connection pads had to be implemented in the design. The connection end had to be widened for these connection pads to be fitted. Finally, the spacing between the wires was made larger so that the chance of the wires accidentally contacting was as low as possible. The result is the final sensing structure seen in figure 2.6.

The idea is that with a four wire measurement the voltages, and consequently the resistances, of these points can be read out. As there are $2 \times 3 = 6$ total measurements to be read out, at least 6 channels need to be used. These resistances can be used to analyse the relative resistance change in these areas of the actuator. The relative resistance change can give an idea of the change in strain in three regions. With that data it should be possible to differentiate contact with the actuator at different points along the actuator.

2.5 Theoretical background

To predict the amount of strain and, consequently, the amount of relative resistance change, a model is put in to place. To make this model understandable, a couple of aspects should be

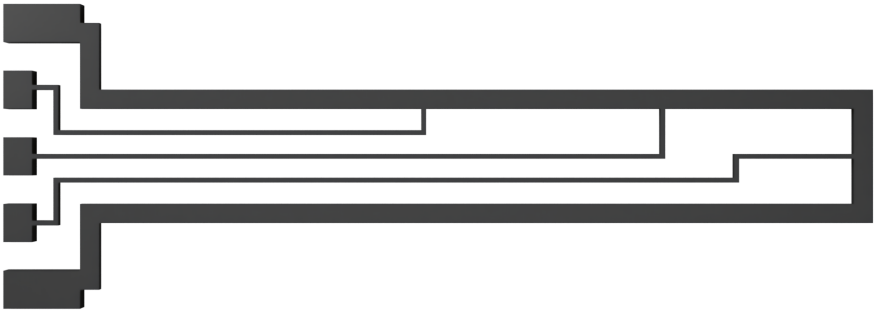

Figure 2.6: New sensor structure

defined. The model assumes the actuator without the pneu-net to behave like a single side clamped bending cantilever. Obviously this is not a completely correct assumption, as there are many factors that diverge somewhat from regular Euler-Bernouilly beam theory, which will be explained later. In figure 2.7 a schematic representation of the actuator bottom plate can be seen with indications of the variables e, the distance of a sensor to the neutral axis of the beam, and the bending angle θ. Because one sensor will have a negative value of e and one a positive value of e, there will be one sensor with a positive strain ϵ and one sensor with a negative strain ϵ, see equation 2.9.

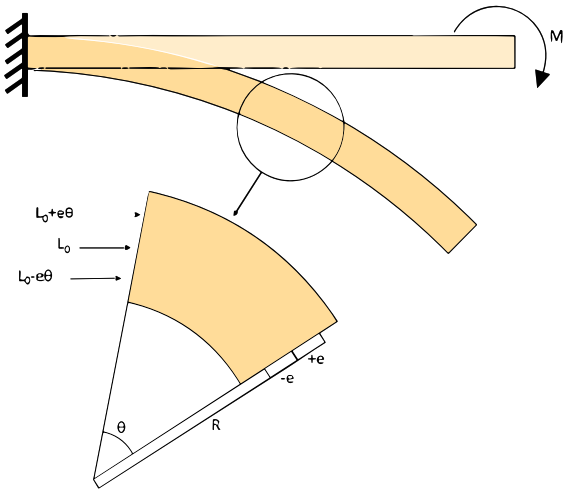

Figure 2.7: View of the theoretical cantilever beam, where e is the distance from the neutral axis to a sensor, and θ the bending angle (from [4])

From figure 2.7 can be deduced that for the length of a deflected beam L_{d} one may write:

$$L_{\mathrm{d}} = L_0 + e \cdot \theta \tag{2.8}$$

The definition of strain says that the strain is equal to the ratio of the deformation to the length in rest due to a force on that body. That fact, together with equation 2.8 can be written as equation 2.9

$$\epsilon = \frac{\Delta L}{L_0} = \frac{L_{\mathrm{d}} - L_0}{L_0} = \frac{L_0 + e \cdot \theta - L_0}{L_0} = \frac{e \cdot \theta}{L_0} \tag{2.9}$$

For a strain gauge, the relative resistance change is directly related to the strain and the gauge factor GF, as is shown in equation 2.10

$$\frac{\Delta R}{R_0} = \epsilon \cdot GF = \frac{e \cdot \theta}{L_0} \cdot GF \tag{2.10}$$

Unfortunately, this gauge factor is different for every material. Where most materials have a linear, straightforward gauge factor, the ETPU used for the sensors has been found to have a highly irregular one, due to its nonlinearities. Doshi et al. [17] have found an approximation as found in equation 2.11

$$\frac{\Delta R}{R_0} = 2.356\epsilon^2 - 1.408\epsilon \tag{2.11}$$

Now we can continue the modeling of the strain in the beam. The bending angle of the beam can be modeled using the equations for a cantilever beam with an intermediate load, with a Young's modulus E and a second moment of inertia I. The situation is shown in figure 2.8. L is the full distance from clamp to the tip of the beam, a is the distance from the clamp to the point of contact and F is the force acting on the beam. Here, x is a point on the x-axis, along L.

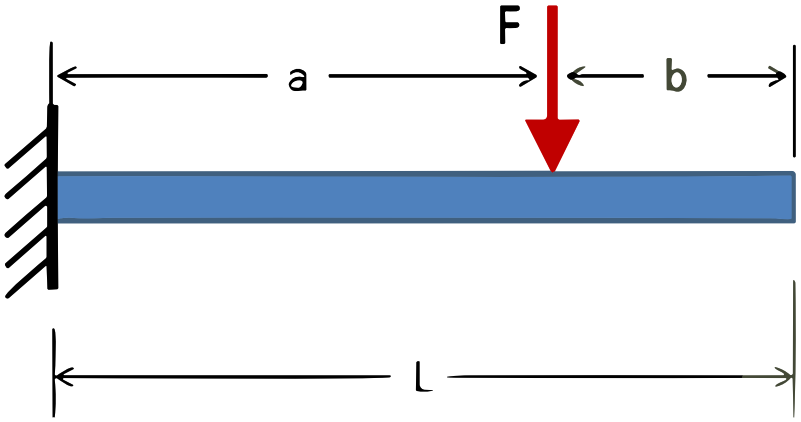

Figure 2.8: Cantilever model with flexible load

The Young's modulus of the beam is a measure of compressive stiffness, which is mostly dominated by the Ninjaflex TPU, as by far most of the beam is made out of that material. For the Ninjaflex TPU the Young's modulus E = 12 MPa. This will be used in calculations, even though E would probably be a bit higher due to the ETPU. The second moment of inertia can be determined using equation 2.12, where w is the width of the beam and h the height or thickness of the beam.

$$I = \iint_R y^2 \, dA = \int_{-\frac{w}{2}}^{\frac{w}{2}} \int_{-\frac{h}{2}}^{\frac{h}{2}} y^2 \, dy \, dx = \int_{\frac{w}{2}}^{\frac{w}{2}} \frac{h^3}{12} \, dx = \frac{wh^3}{12} \tag{2.12}$$

Then, from Mechanics of Materials [18] the following bending angle equations can be deducted for this scenario:
for $0 \leq x \leq a$:

$$\theta = \frac{F \cdot x}{2E \cdot I}(2a - x) \tag{2.13}$$

and for $a \leq x \leq L$:

$$\theta = \frac{F \cdot a^2}{2E \cdot I} \tag{2.14}$$

Substituting these into equation 2.9 gives the strain at each point along the beam. However, we would like to know the total strain over the three sensor segments: short, medium and long.

This can be done by integrating over these segments with regards to x. Which would lead to equations 2.15, 2.16 and 2.17 for the short, medium and long segment respectively. This is only for the case in which the segment falls completely within a: $0 \leq x \leq a$. Because there is no dependency on x in equation 2.14, all integrals will lead to the expression in equation 2.18 for $a \leq x \leq L$. Because of these two different equations for every segment, it was decided to only analyse the cases of a = 25,50 and 75 mm, so that every segment only includes one of the two integrals. Because it makes no difference if equation 2.11 is evaluated between the integral or not, it is done outside of the integral, to make it more readable.

$$\epsilon_{\text{short}} = \int_0^{\frac{L}{3}} \frac{e \cdot F \cdot x(2a-x)}{2E \cdot I \cdot L}\, dx = \frac{e \cdot F \cdot L(9a-L)}{162E \cdot I} \tag{2.15}$$

$$\epsilon_{\text{medium}} = \int_{\frac{L}{3}}^{\frac{2L}{3}} \frac{e \cdot F \cdot x(2a-x)}{2E \cdot I \cdot L}\, dx = \frac{e \cdot F \cdot L(27a-7L)}{162E \cdot I} \tag{2.16}$$

$$\epsilon_{\text{long}} = \int_{\frac{2L}{3}}^{L} \frac{e \cdot F \cdot x(2a-x)}{2E \cdot I \cdot L}\, dx = \frac{e \cdot F \cdot L(45a-19L)}{162E \cdot I} \tag{2.17}$$

and for $a \leq x \leq L$ for all segments:

$$\epsilon = \int_0^{\frac{L}{3}} \frac{e \cdot F \cdot a^2}{2E \cdot I \cdot L}\, dx = \int_{\frac{L}{3}}^{\frac{2L}{3}} \frac{e \cdot F \cdot a^2}{2E \cdot I \cdot L}\, dx = \int_{\frac{2L}{3}}^{L} \frac{e \cdot F \cdot a^2}{2E \cdot I \cdot L}\, dx = \frac{e \cdot F \cdot a^2}{6E \cdot I} \tag{2.18}$$

Using Matlab [19] and equation 2.11 this can be modeled as a relative resistance change over time. As an input, we feed a 1N, 0.3 Hz sine wave force signal. This results in figures 2.9, 2.10 and 2.11. These figures show only the graphs for one sensor, because the other will have the same graphs but inverted. These figures show that there become larger differences in relative resistance change when the pressure point is shifted further to the tip of the beam.

2.6 Conclusion

In this chapter, first the requirements for the new sensor structure were formulated. Then the current actuator design was explained. Based on the new actuator requirements a new sensing structure design was brought forward. For this design the topics of sensor type and nonlinearity compensation were discussed. Eventually, a piezoresistive sensing structure, using a differential pair for nonlinearity compensation, was selected as the most suitable sensing candidate. The final sensing structure can be seen in figure 2.6. To predict the behaviour of the sensor, an analytical model was derived for estimating the amount of strain in the beam sections. The results can be seen in figures 2.9, 2.10 and 2.11.

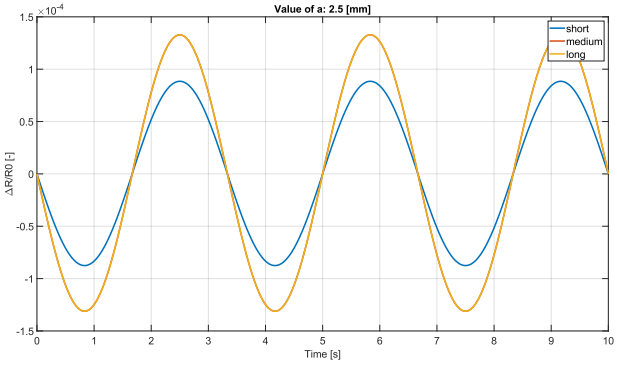

Figure 2.9: Model for a=25 mm

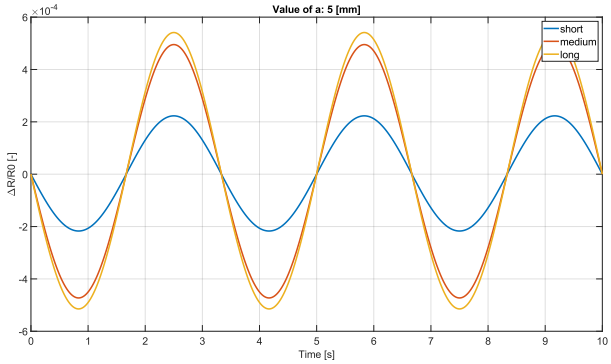

Figure 2.10: Model for a=50 mm

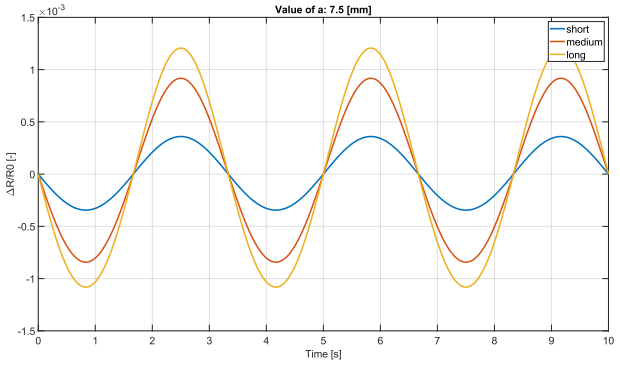

Figure 2.11: Model for a = 75 mm

3 3D printing

3.1 Introduction

In this chapter the fabrication process using 3D printing will be discussed. First, the 3D printer will be covered. Then the printing software will be explained and lastly the challenges of 3D printing will be discussed.

3.2 Fused Filament Fabrication (FFF) 3D printer

It has been established that for the actuator and its sensors two different materials need to be used. To be able to 3D print the whole model in one go, a 3D printer that can print multiple materials is necessary. The Diabase H-series multi material FFF 3D printer (Diabase Engineering, Longmont, CO, USA) is able to do this. This printer uses the so called fused filament fabrication process. This process includes feeding a continuous filament of thermoplastic material. The thermoplastic is heated in an extruder nozzle, melting the thermoplastic so that it can be deposited on the printing bed [20]. This 3D printer has access to a total of 5 extruders, which means it is capable of using 5 different filaments in one print. In figures 3.1 and 3.2 the Diabase H-series 3D printer that was used is shown.

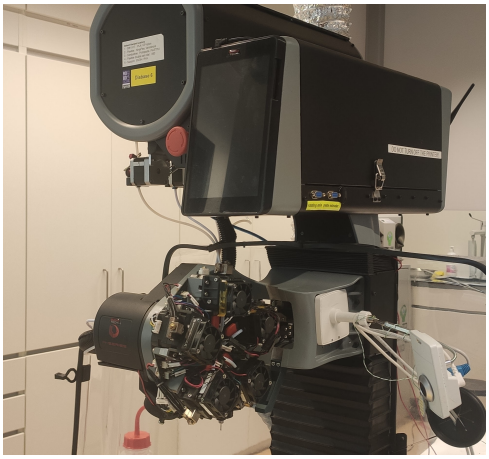

Figure 3.1: Diabase H-series 3D printer

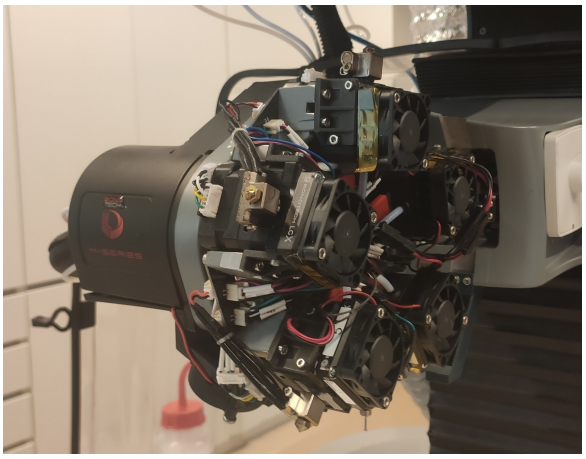

Figure 3.2: Diabase H-series nozzlehead

3.3 Slicing

After the construction of the model using Fusion 360 [21] the model is passed on to the slicer, which is a program that takes a model and converts it into instructions for the 3D printer. The slicing software that was used is Simplify3D [22]. Most of the settings were identical to the settings used for the previous actuator design.

Parameter	TPU (Ninjaflex)	ETPU (PI-ETPU 85-700+)	PVA
Extrusion multiplier	1.15	1.00	0.85
Nozzle diameter	0.4 mm	0.4 mm	0.4 mm
Layer height	0.2 mm	0.2 mm	0.2 mm
Temperature	235 °C	205 °C	185 °C
Printing speed	2000 mm/min	2000 mm/min	2000 mm/min

Table 3.1: Slicer setting overview

In table 3.1 the most important slicer settings are shown.

3.4 Printing

Because we are just interested in a proof of concept, not the whole actuator was printed. The pneu-net pressure chambers were removed, and only the bottom plate, where the sensing structure is situated, was printed. However, even with that reduced printing complexity printing the concept design using the Diabase 3D printer introduced some unexpected issues. The first of which was that blobs of Ninjaflex [10] filament began forming at places where the nozzle lifts off. This was primarily an issue because these liftoff places were often close to an ETPU [11] wire. This often caused the ETPU material of top and bottom sensor to mix with each other, establishing a connection between the differential sensor. This makes the sensor useless. For this reason the actuator design was made wider and between the wires larger spacings were introduced.
Another issue that the first couple of models had was that their bottom strain gauge was printed directly on the printing bed. This resulted in a large difference in resistance between the top and bottom sensors. This problem was solved by adding a couple of layers of Ninjaflex, before the first ETPU strain gauge layer. For this method to be successful, it was important that the bottom layer would not stick to the printing bed. That is why a support material was used. The material used for this was PVA, which is a water soluble 3D printing filament, so it is easy to separate from the rest of the print. This material was printed like a bed of a few layers high. The resulting print can be seen in figure 3.3, where the ETPU is black, the Ninjaflex brown and the PVA grey. In this figure, it can be seen that the wider part extends a bit beyond the connection pads. This is so that the beam can be clamped better during measurements. The final dimensions of the beam, so ignoring the clamping and connection space, are: 75mm long by 18mm wide by 4.2mm high.

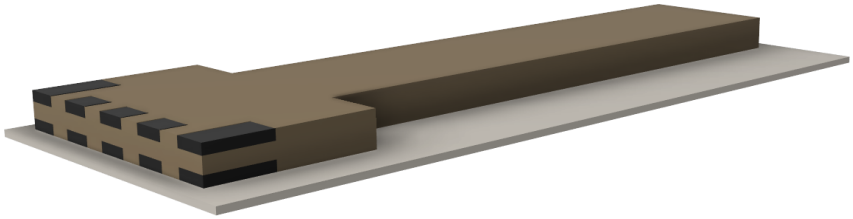

Figure 3.3: Final print model. In brown Ninjaflex TPU, in black PI-ETPU and in white PVA

3.5 Characterisation

Now that the actuator plate has been printed, it is necessary to name a couple of important parameters that will be used during the rest of the report. In figure 3.4 L_1 is the length from the clamp to the first senor wire, which is 25mm. L_2 is two thirds of the sensor length, which is 50mm and L_3 is the full length of the sensor, at 75mm. The region between the clamp and the first sensor is defined 'short', the region between L_1 and L_2 is defined 'medium' and the region between L_2 and the end is defined 'long'.

3.6 Conclusion

This chapter covered the fabrication method and the characterisation of some important parameters. The designed model has been printed using a Diabase H-series FFF 3D printer. The settings used for printing are given as well. Additionally, the experienced problems with 3D printing have been explained. Finally, the terminology of some important paramaters were defined.

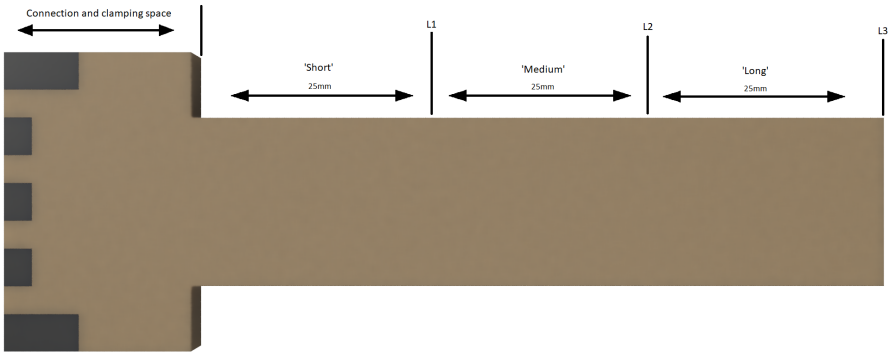

Figure 3.4: Sensor definitions

4 Measurement Setup

4.1 Introduction

In this chapter the measurement setup is explained and illustrated.

4.2 Setup

For the measurements, four main resources have been used. First off, a DC current source (HP E3631A) has been used. Secondly, a linear actuator has been used to apply a force on the beam. The device that was used is a SMAC actuator (LDL40-100-31-3F, SMAC Moving Coil Actuator (2019)). Thirdly, a load cell (LCMFD-50N) was used to measure the amount of force the SMAC actuator puts out. The last device that was used is the DEWE-43A (Dewesoft). This device has 8 analog input and 8 digital input channels available.
Before testing began, the sample seen in figure 4.1 was prepared with wires. These wires have been soldered into the conductive ETPU to connect the sensor to the DEWE-43A, so that the sensor data can be read out. There are four wires that are sticking out at the side of the beam in

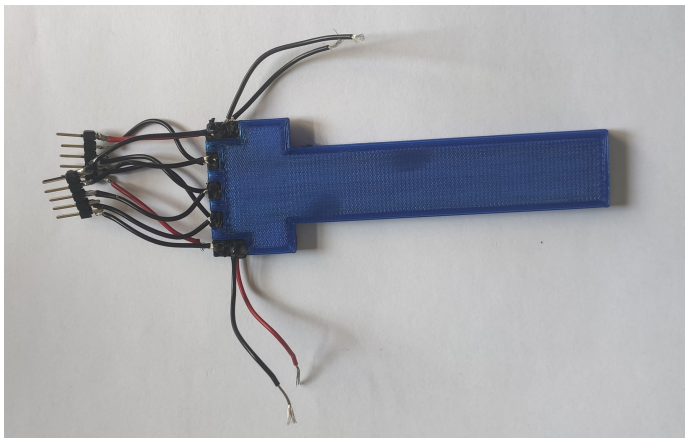

Figure 4.1: Sample used for testing

figure 4.1. Those are for connection to the current source. Ten more wires can be seen in figure 4.1, five for both the bottom and top sensor. Three of those five are for the added sensors, while the remaining two are for both the strain gauge ends. This means a total of ten voltages could be read out simultaneously. However, only eight channels are available. One of these channels is connected to the load cell. That leaves seven channels. Six of these will be used to measure the sensor data and the last one will be used to measure the output voltage of the current source. In figure 4.2 the used channels can be seen. It is important to note that all channels shared the same ground, the one that is in figure 4.2. The impedance of power source in the voltage measurements is very high, so that the resistance of the wires from the strain gauge to the connection pads do not influence the measurement. That means every channel is an effective four wire measurement, giving high accuracy of the measured voltages.

1. Input voltage
2. Top short
3. Top medium
4. Top long
5. Bottom long

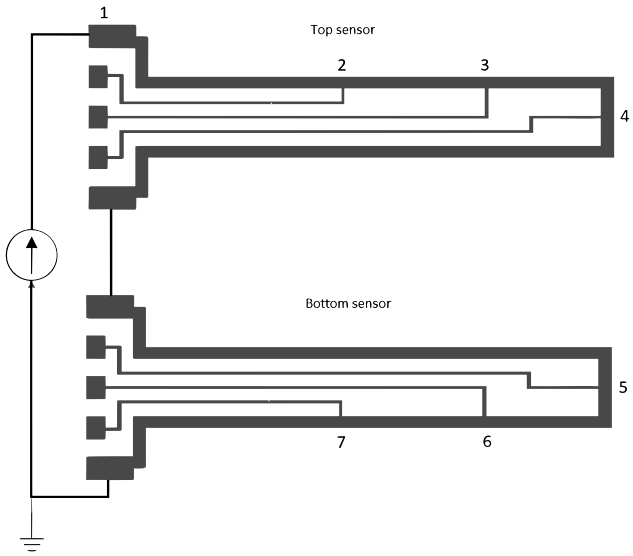

Figure 4.2: Schematic of measurement setup connection

6. Bottom medium
7. Bottom short

The measurements were done with the beam clamped vertically with the SMAC actuator pushing on it horizontally, as in figure 4.3. The current source was set to 1mA, so that the sample is not under a too high voltage, for every measurement. The SMAC actuator was driven using a 0.3Hz sine wave with a variable maximum force. The actuator pushes on the bottom part of the beam. This means the bottom sensors have a positive distance to the neutral axis and the top sensors have a negative distance to neutral axis when pushing.

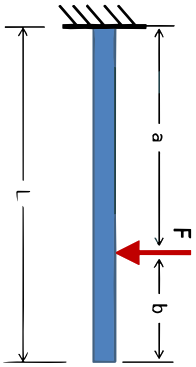

Figure 4.3: Measurement setup

The first measurements were done as illustrated in figure 4.3, applying a force on different points along the beam, like the analytical model does as well. Later measurements were also done using a fitting u-shaped container, like a bucket, at the tip of the beam. This was used to experiment with the actuator not only pushing, but also pulling at the sample.

In figure 4.4 the real life setup can be seen. In the foreground on the left the SMAC actuator and the sample beam on the right. In the background the DEWE-43A and a lot of wires can be seen.

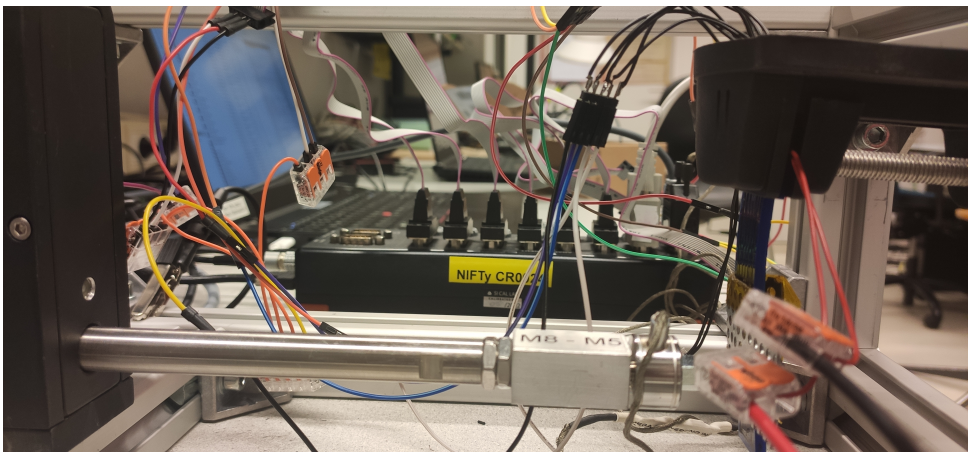

Figure 4.4: Measurement setup

4.3 Conclusion

In this chapter, Afterwards, the measurement setup is described in detail. In figure 4.2 the connection scheme can be found and in figure 4.4 the real life setup can be seen.

5 Results

5.1 Introduction

In this chapter the results of multiple experiments are presented, which are then analysed for sensor characterisation. First, the resistance of the sensors and the build quality are discussed, after which the results from experiments are presented.

5.2 Build quality

To validate that there were no errors in the print, either no connection or connection between the top and bottom sensor, a 4 wire resistance measurement was done. The results are shown in table 5.1. The measurements were taken over the whole beam up until the measurement point. This means all measurements include the intermediate segments. Thus the right column of table 5.1 has the corrected value, the measured value minus the resistance value of the intermediate segments.

Segment	**Measured resistance**(kΩ)	**Corrected resistance of the segment**(kΩ)
Top short	0.75	0.75
Top medium	1.16	0.41
Top long	1.62	0.46
Bottom short	0.76	0.76
Bottom medium	1.18	0.42
Bottom long	1.85	0.67

Table 5.1: Sensor resistances

When we take a look at the corrected column in table 5.1 we can see that the resistance of the short sections are a bit higher than the rest. This is due to the fact that the strain gauge is longer than the sensor sections, it also includes the length of the clamping space. This extra length is about 2 cm, so we do expect $\frac{0.25+0.2}{0.25} = 1.8$ times as much resistance there. So that does look correct. This can be accounted for in the data processing. The only odd one out is the bottom long sensor, which has about a 1.5 times as high a resistance as the rest. This could be due to some pollution in the print or a less than optimal connection to the connection pad. However, this is usable, as long as the relative resistance change is proportional to the higher resistance. A continuity check was done as well, to ensure there is no connection between bottom and top sensors. The result was positive: no connection between the sensors. Overall, it is good to see that the resistances for the bottom and top sensor are rather comparable.

5.3 Experiments

In this section the experiment results are shown. For all of these, the SMAC actuator was force controlled with a sine wave of 0.3Hz with an amplitude of 1N. Because both strain gauges are connected to the same current source in series and the voltages get divided, it is good to grab figure 5.1 again.

This leads to the following equations, with i the set current of 1 mA:

$$R_2 = \left(\frac{V_1 - V_2}{i}\right) \tag{5.1}$$

$$R_3 = \frac{V_2 - V_3}{i} \tag{5.2}$$

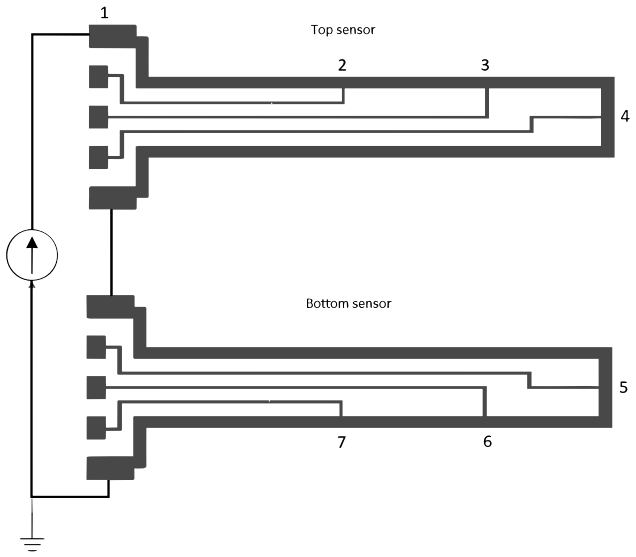

Figure 5.1: Schematic of measurement setup connection

$$R_4 = \frac{V_3 - V_4}{i} \tag{5.3}$$

$$R_5 = \frac{V_5 - V_6}{i} \tag{5.4}$$

$$R_6 = \frac{V_6 - V_7}{i} \tag{5.5}$$

$$R_7 = \left(\frac{V_7 - 0}{i}\right) \tag{5.6}$$

Setting a baseline for each voltage when the sample is at rest, gives a value of R_0 for every measuring point. This R_0 can then be related to the voltage at any given moment to get the relative resistance change $\frac{\Delta R}{R_0}$.

5.3.1 Intermediate load

The first experiment is one with intermediate loading. This experiment uses the same actuation at three different points along the beam. This gives a measure of how the sensors will respond to forces in different segments of the beam. The results of the bottom and top sensor are shown as well as the differential result, meaning bottom - top results. This gives figure 5.2 for a force close to the clamp, figure 5.4 for a force at the tip of the beam and figure 5.3 for a force in the middle of the other measurements.

The bottom figure in figure 5.2 shows that for the differential measurement the three segments are not very distinguishable. This is expected, as figure 2.9 expects the medium and long segments to coincide, with little difference to the short segment. At some points the relative resistance change is even higher for the short segment than the other two segments. It could be that this is because the bending angle θ is very small for this scenario.

A better result can be seen in figure 5.3. When this figure is compared to the theoretical model related to it, figure 2.10, it fits very nicely. It can be seen that the resistance change in the long segment is largest, with the medium segment second. With a little more distance to the other two is the short segment, just like the theoretical model predicts.

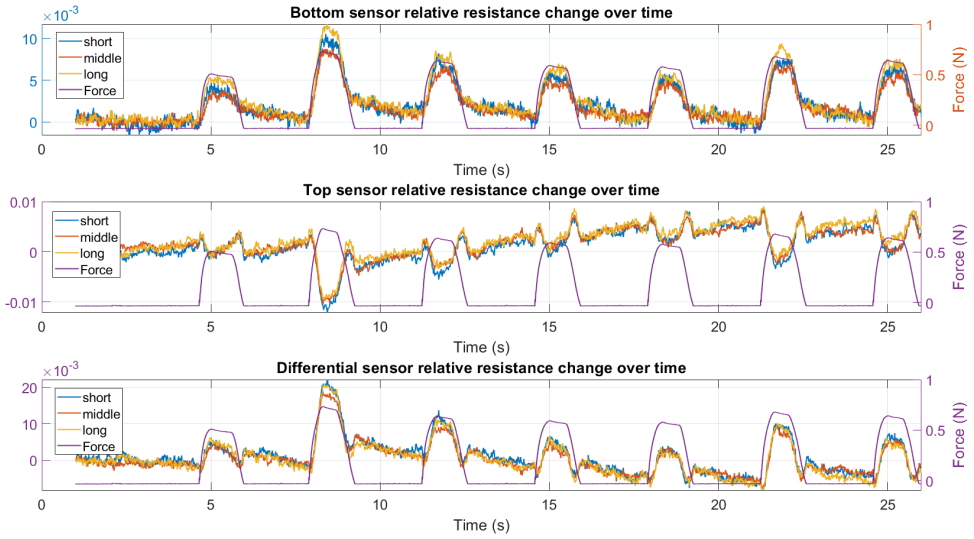

Figure 5.2: Relative resistance change with force acting at $\frac{1}{3}$rd of the length

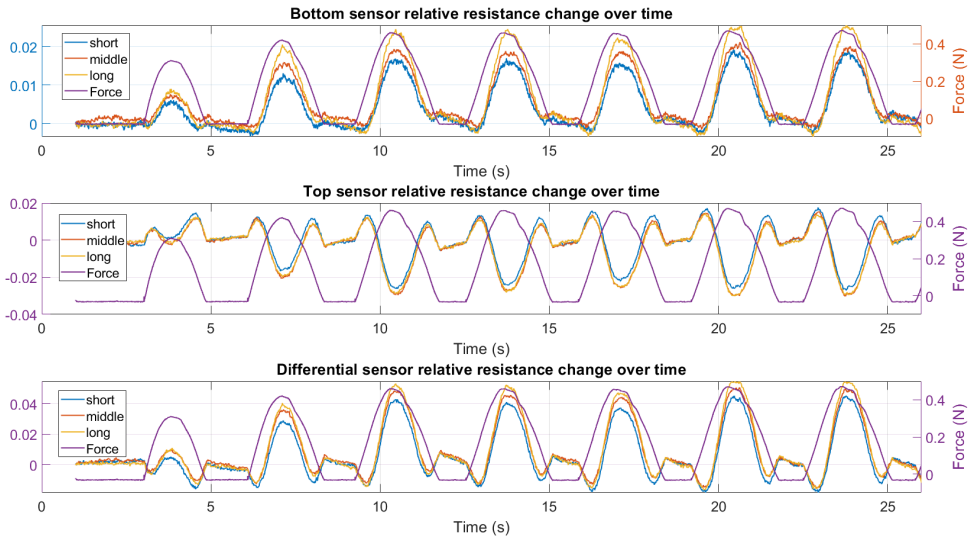

Figure 5.3: Relative resistance change with force acting at $\frac{2}{3}$rd of the length

The bottom graph in figure 5.4 shows a similarly shaped result to figure 5.3. Only the distance from the long and medium segments to the short segment is bigger and the scale of the relative resistance scale is smaller. This still fits the theoretical model found in figure 2.11, actually even better than the previous one. However, the theoretical models don't see a difference in scale.

5.3.2 push-pull configuration

Not only is there an interest in the response to a one sided contact, there is also an interest in the two sided contact response. This has been analysed using a small, fitting bucket that encloses the tip of the beam, so that the actuator can exert a force in both the positive and negative direction on the sample. Mostly this is done to investigate if pulling on the sample has the same effect as pushing on the sample, or if these are different.

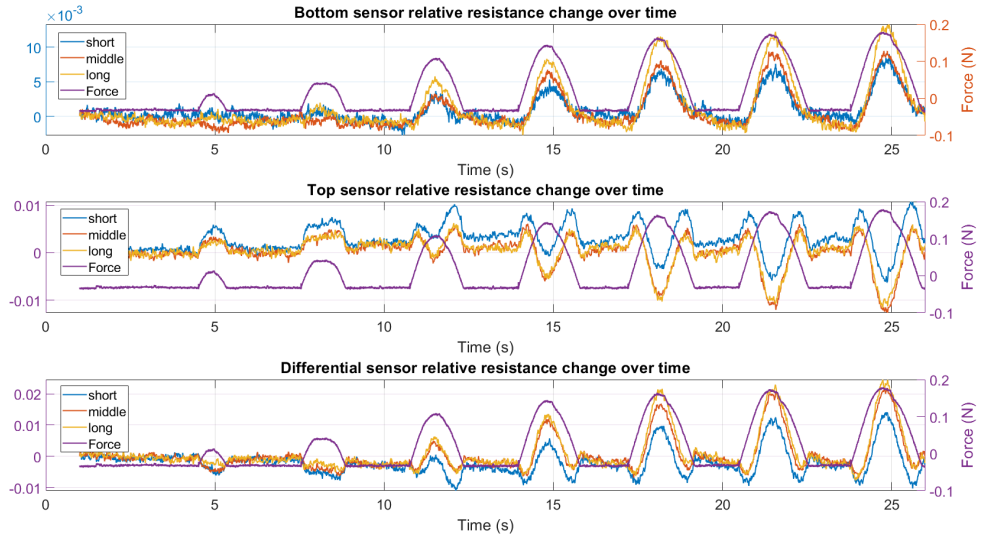

Figure 5.4: Relative resistance change with force acting on the tip of the beam

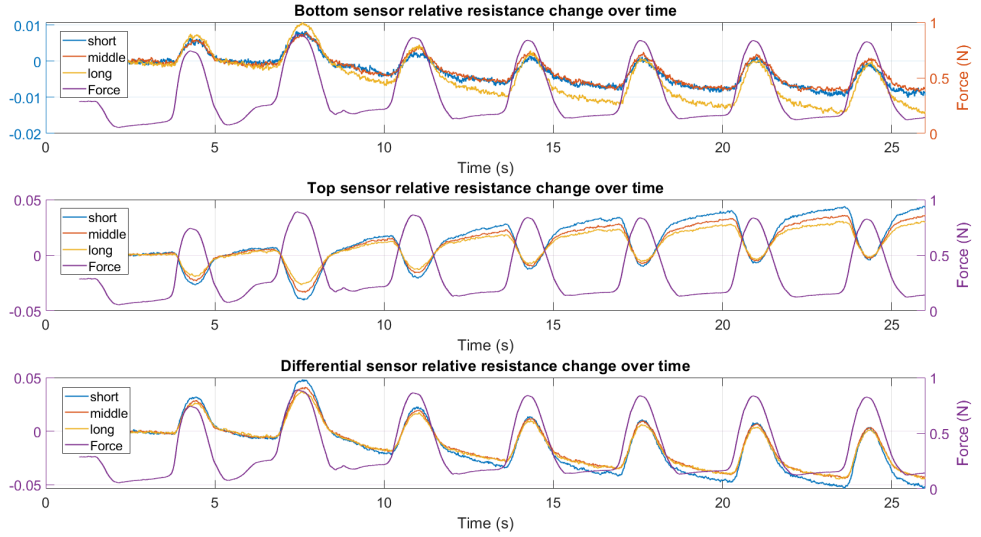

Figure 5.5: Relative resistance change in push-pull configuration

Figure 5.5 immediately shows that pulling does not have the same effect as pushing, as there are only half sines visible for the pushing part of the movement. This is probably the result of the relaxation after a push, which makes the relative resistance drop very gradually, and the 1N pull is not enough to get a sine like response after. It also shows that because of the pulling the relative resistance starts drifting down.

When comparing figure 5.5 with figure 5.6, it can clearly be seen that a larger force acting on the beam results in a larger relative resistance change. However, the difference is larger than 2 times magnification.

Because this experiment uses both sides of the force sine wave, it can best be used for comparing the achieved results to the theoretical results. In figure 5.7 the theoretical curve for $a = 75$ mm can be seen for each segment versus the experimental fit of these segments.

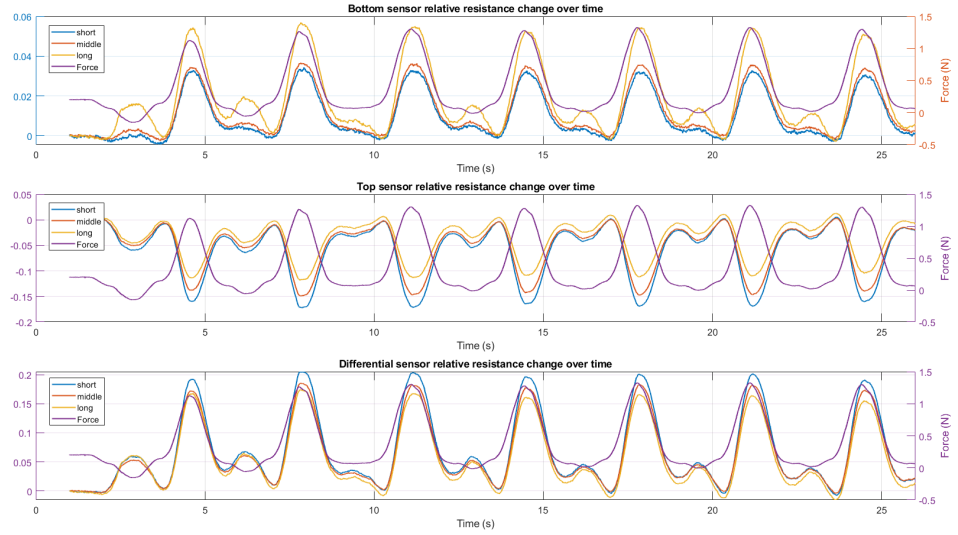

Figure 5.6: Relative resistance change in push-pull configuration with twice the force applied

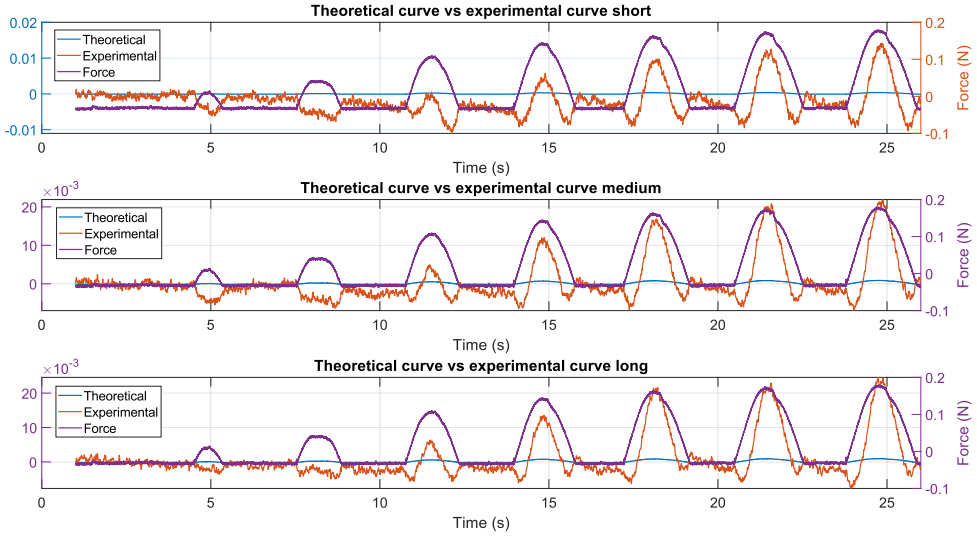

Figure 5.7: Theoretical relative resistance change vs experimental differential resistance change

It can clearly be seen that these curves differ a lot. Even though the experimental curvature is as expected, the amplitude is about 10 to 20 times as high as expected. This might be due to a combination of inaccuracy in the Young's modulus of the sample and the fact that the theoretical model is better applicable for stiffer materials under a larger force. However, the higher amplitude is not necessarily a bad thing, as this might be beneficial for the sensitivity of the sensor.

Overall, what these results show is that the differential measurement is mostly dominated by the bottom sensor. This is to be expected, as the actuator is pushing on the bottom side of the beam, and thus the force will be experienced to a higher degree. However, the differential results show better, more linear results than the bottom sensor alone.

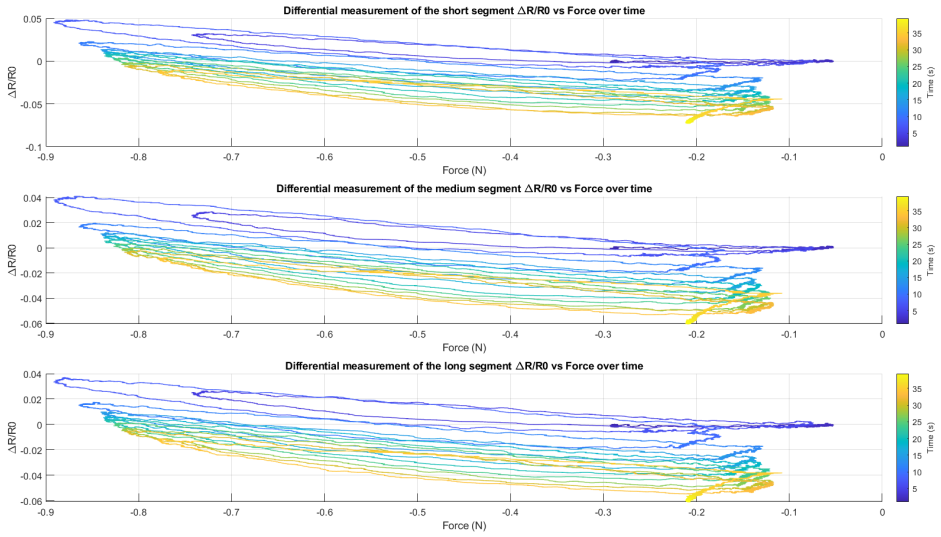

Figure 5.8: Relative resistance change of all segments versus the applied force over time

This experiment also gives insight into the behaviour of the sensors over time. In figure 5.8 it can be seen that even though the actuated force over every cycle remains largely the same, the relative resistance change drifts away gradually with a bit of hysteresis.

5.4 Conclusion

This chapter showed the achieved results from two different experiments. In figures 5.2, 5.3 and 5.4 the results from the first experiment can be seen. These results are quite similar to what was expected for this experiment. In figure 5.5 the result for the push-pull experiment is shown. It shows that the relative resistance change is apparent almost fully by the pushing of the linear actuator, and that pulling on the beam does not show similar effects. In figure 5.7 the theoretical curves were compared to the experimental curves. This showed a large deviation. This could have a number of reasons, which will be discussed in the next section.

6 Discussion

Now that all results have been presented, it is time to analyse them.

6.1 Relation to theoretical model

For both experiments it was found that the results don't quite fit the models established in chapter 4. The issue that arose in the first experiment, is that forces applied close to the clamp make it difficult to see any difference between the segments. Even though this is not the wanted result, this could be used for recognition of the point of contact. This is not very accurate though.
The issue in the order of magnitude of the relative resistance change in the experiments is likely due to the fact that the beam bends too much for regular Euler-Bernouilli beam theory to apply. This is because the TPU acts almost like a hyperelastic material [23]. Also, deviations could occur because only the Young's modulus of the TPU is considered, while the ETPU does have an influence on that number. In the future, an alternative model for larger deflections could be analysed, which would likely fit the experimental values better.

6.2 Usability

What the results in figure 5.2, 5.3 and 5.4 show is that the sensors can be used to make the distinction of the contact region. This can be done by relating the relative resistance change of the three different segments, because there is a difference in the amount of resistance change between the points of force engagement. However, it is very hard to distinguish contact with a certain segment when the force is unknown, because a larger force will also increase the relative resistance change. The downside is, that this is only the case when the amount of force is known. In that case it is very hard to give distinction of the point of force engagement. That also makes it impossible to determine the interaction force with the environment consistently. Additionally, these sensors can show quite some drift and hysteresis when force is acted upon the beam both in positive and negative direction. Also, it is unknown how attaching the pneu-nets will influence these sensors. The pneu-nets will influence the strain in certain places when bending, because of the pressure that the chambers will push against each other with. Taking all of this in mind, it is difficult to say if the concept of these sensors will work in a soft robotic pneu-net actuator.

7 Conclusion

7.1 Conclusion

This report shows a concept of a 3D printed soft robotic beam with integrated sensing. This beam is the foundation for a soft robotic actuator with angle sensing. The sensing structure is composed of two strain gauges from conductive TPU with three branching sensor wires each. These wires had the goal of sensing the interaction force with the environment. This design was successfully converted to a working sample using a multi material FFF 3D printer.
The expected behaviour of the beam has been modeled using Euler-Bernouilli beam theory. It was found that this might be suboptimal due to the hyperelastic properties of the beam. A more accurate model of the beam would help increase understanding in the experimental response. What this paper shows is that this type of sensor can be 3D printed using multi material 3D printing. However, it does not give a positive conclusion as to the usability of this sensor in the future. That is why it could be an option to investigate this type of sensor with capacitive sensing instead of piezoresistive sensing.

Bibliography

[1] J. Walker, T. Zidek, C. Harbel, S. Yoon, F. S. Strickland, S. Kumar, and M. Shin, "Soft robotics: A review of recent developments of pneumatic soft actuators," *Actuators*, vol. 9, 3 2020.

[2] C. Majidi, "Soft-matter engineering for soft robotics," *Advanced Materials Technologies*, vol. 4, 2 2019.

[3] T. Ashuri, A. Armani, R. J. Hamidi, T. Reasnor, S. Ahmadi, and K. Iqbal, "Biomedical soft robots: current status and perspective," *Biomedical Engineering Letters*, vol. 10, pp. 369–385, 8 2020.

[4] G. Wolterink, S. Kolkman, and G. Krijnen, "3d printed soft robotic actuator with embedded strain sensing for position estimation," *Proceedings of IEEE Sensors*, vol. 2022-October, 2022.

[5] M. Schouten, G. Wolterink, A. Dijkshoorn, D. Kosmas, S. Stramigioli, and G. Krijnen, "A review of extrusion-based 3d printing for the fabrication of electro- a nd biomechanical sensors," *IEEE Sensors Journal*, vol. 21, pp. 12900–12912, 6 2021.

[6] K. Elgeneidy, G. Neumann, M. Jackson, and N. Lohse, "Directly printable flexible strain sensors for bending and contact feedback of soft actuators," *Frontiers Robotics AI*, vol. 5, 2018.

[7] F. Aljaber, A. Hassan, I. Vitanov, and K. Althoefer, "Curvature and contact sensing with optical waveguides for soft silicone pneumatic actuator," *2022 IEEE 5th International Conference on Soft Robotics, RoboSoft 2022*, pp. 859–864, 2022.

[8] soft robotics toolkit, "Pneunets bending actuators." https://softroboticstoolkit.com/book/pneunets-bending-actuator.

[9] B. Mosadegh, P. Polygerinos, C. Keplinger, S. Wennstedt, R. F. Shepherd, U. Gupta, J. Shim, K. Bertoldi, C. J. Walsh, and G. M. Whitesides, "Pneumatic networks for soft robotics that actuate rapidly," *Advanced Functional Materials*, vol. 24, pp. 2163–2170, 4 2014.

[10] NinjaTek, "Ninjaflex 3d printing filament." https://ninjatek.com/wp-content/uploads/NinjaFlex-TDS.pdf.

[11] P. innovation, "Palmiga innovation." https://palmiga.com.

[12] BCN3D, "Technical data sheet pva." https://3dprint.pe/wp-content/uploads/2018/09/TDS_BCN3D_Filaments_PVA.pdf.

[13] H. Jonkers, "3d printed electronics," January 2022.

[14] H. Qi and M. Boyce, "Stress–strain behavior of thermoplastic polyurethanes," *Mechanics of Materials*, vol. 37, no. 8, pp. 817–839, 2005.

[15] G. Wolterink, R. Sanders, B. J. van Beijnum, P. Veltink, and G. Krijnen, "A 3d-printed soft fingertip sensor for providing information about normal and shear components of interaction forces," *Sensors*, vol. 21, 7 2021.

[16] M. Schouten, B. Prakken, R. Sanders, and G. Krijnen, "Linearisation of a 3d printed flexible tactile sensor based on piezoresistive sensing," 2019.

[17] A. A. . Ajinkya and . Doshi, "3d printed interaction force sensors for robotic fingers," 2021.

[18] J. Gere and B. Goodno, *Mechanics of Materials*. Cengage Learning, 2008.

[19] Mathworks, "Matlab." https://mathworks.com/products/matlab.html.

[20] Wikipedia, "Fused filament fabrication." https://en.wikipedia.org/wiki/Fused_filament_fabrication.

[21] Autodesk, "Fusion 360." https://fusion.online.autodesk.com.

[22] "Simplify3d." https://simplify3d.com.

[23] C.-H. Liu, Y. Chen, and S.-Y. Yang, "Quantification of hyperelastic material parameters for a 3d-printed thermoplastic elastomer with different infill percentages," *Materials Today Communications*, vol. 26, p. 101895, 2021.